Tungsten-based bcc-superalloys

Knowles, Sandy; Dye, David; Dodds, Russel J; Watson, Andy; Hardie, Christopher D; Humphry-Baker, Samuel A

DOI:
10.1016/j.apmt.2021.101014

Document Version
Peer reviewed version

Citation for published version (Harvard):
Knowles, S, Dye, D, Dodds, RJ, Watson, A, Hardie, CD & Humphry-Baker, SA 2021, 'Tungsten-based bcc-superalloys', *Applied Materials Today*, vol. 23, 101014. https://doi.org/10.1016/j.apmt.2021.101014

Tungsten-based bcc-superalloys

Alexander J Knowles[a,b,d,*], David Dye[a], Russel J Dodds[a], Andy Watson[c], Christopher D Hardie[d], Samuel A Humphry-Baker[a]

[a] *Department of Materials, Imperial College, South Kensington, London SW7 2AZ, UK*
[b] *School of Metallurgy & Materials, University of Birmingham, Birmingham, B15 2SE, UK*
[c] *Hampton Thermodynamics Limited, Hampton, TW12 1NL, UK*
[d] *Culham Centre for Fusion Energy, Abingdon, Oxfordshire, OX14 3DB, UK*

Abstract

Applications from nuclear energy to rockets and jet engines are underpinned by advanced high temperature materials. Whilst state of the art, the performance of current nickel-based superalloys is fundamentally limited to Ni's melting point, T_m = 1455°C. Here, we develop an analogous superalloy concept but with superior high temperature capability by transitioning to a bcc tungsten base, T_m = 3422°C. This strategy involves reinforcing bcc β-W by β' TiFe intermetallic compound, which results in impressive high temperature compressive strengths of 500 MPa at 1000°C. This bcc-superalloy design approach has wider applicability to other bcc alloy bases, including Mo, Ta, and Nb, as well as to refractory-metal high entropy alloys (RHEAs). By investigation of the underlying phase equilibria, thermodynamic modelling, characterisation and mechanical properties, we demonstrate the capability of ternary W-Ti-Fe tungsten-based bcc-superalloys as a new class of high temperature materials.

Keywords: High Temperature Materials, Tungsten, Phase Equilibria, Intermetallics, Precipitation

1. Introduction

High temperature applications, from fusion energy and next-generation fission reactors, to jet engines, rockets and concentrated solar power, are all underpinned by advanced materials. Materials innovations are essential to continue to improve performance and efficiency, and in many cases are depended upon as enabling technologies. In many such applications the materials of choice are nickel-based superalloys due to their exceptional high temperature strength and creep resistance, which is the result of the face-centred-cubic (fcc) γ Ni matrix being strengthened by precipitates of ordered-fcc γ' Ni_3Al intermetallic compound [1, 2]. A strategy to improve temperature capability is to increase melting temperature (T_m), which has guided moves away from a Ni base (T_m = 1455°C), to Co (1495°C) [3], and even Pt (1768°C) [4] and Ir 2466°C [5], however, these either offer only limited temperature improvements, or are prohibitively expensive, Figure 1. In seeking greatly higher melting points, the cost-effective body-centred-cubic (bcc, β) refractory metals Nb, Mo, Ta and W[1] with melting points of 2477-3422°C are the most obvious candidates, Figure 1.

Tungsten, the highest melting point metal (3422°C) has a long history of use in high temperature applications, from incandescent light bulb filaments, to friction

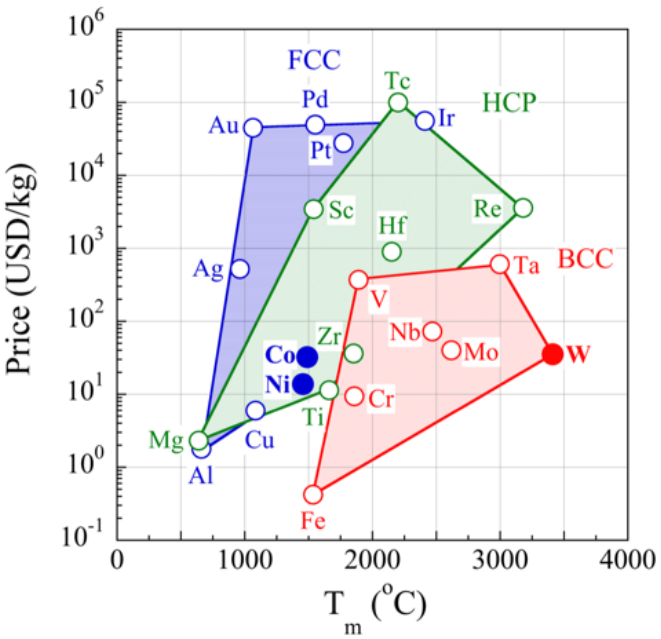

Figure 1: (a) Cost ($/kg) vs melting point (°C), comparing face-centred-cubic (fcc), hexagonal-close-packed (hcp), and body-centred-cubic (bcc) metals [*Underlying data in Appendix, Supplementary Table S1*].

*Corresponding Author. a.j.knowles@bham.ac.uk

[1] It should be noted that we use the definition "bcc β-W" for consistency with the β-Ti and β' TiFe phases, this is in contrast to tungsten literature where β-W is A15 and α-W bcc.

stir welding and space applications including, rocket nozzles, nuclear electric / arcjet thrusters, heat exchangers, as well as in nuclear fusion for the divertor and first wall shielding [6, 7]. Great improvements have been achieved for W, based upon the exploitation of thermo-mechanical and cold-working to give highly refined grain structures, utilising potassium bubble pinning [8], fine carbide particles [6] and increased dislocation densities [9]. Alloying has been hugely successful in W-Re alloys, that achieve an unusual combination of both solid-solution strengthening and toughening [6, 10]. Tungsten heavy alloys are liquid phase sintered alloys consisting of tungsten particles dispersed in a matrix of a lower melting point transition metal [11]. Common matrix formulations include Ni-Fe (Densimet) and Ni-Cu (Inermet) [12]. In these alloys the tungsten particles are broadly spherical, $10-50\,\mu$m in diameter, and comprise 98-80 wt.% of the material. The presence of the Ni-based matrix improves ductility, with failure strains of 5-30% and K_{IC} values of 50-200 MPa.m$^{1/2}$, depending on the size, content and contiguity of the W particles [13]. The matrix also reduces manufacturing cost, due a lowering of the sintering temperature to 1400 °C. Applications include kinetic penetrators [11], gamma ray shielding [14], and are recently being considered for fusion reactors [12, 15]. However, conventional tungsten alloys do not exploit the key design strategy behind nickel-based superalloys, of ordered intermetallic precipitate reinforcement as a means to develop high temperature strength and creep resistance.

Here we consider the opportunity to take inspiration from fcc nickel based superalloys, and to create refractory metal based 'bcc superalloys'. A refractory metal bcc superalloy needs to exploit a reinforcing second-phase with an ordered-bcc β' crystal structure. Hundreds of intermetallic compounds adopt β' structures of the types: CsCl B2 (*Prototype & Strukturbericht structure*), $AlCu_2Mn$ $L2_1$ or BiF_3 $D0_3$. However, critically few β' intermetallics coexist with a bcc refractory metal to give the $\beta+\beta'$ intermetallic two-phase equilibria necessary. There have been notable achievements toward bcc-superalloys in the frameworks of compositionally complex alloys (CCAs): Mo-NiAl [16], Nb-Pd$_2$HfAl [17], Fe(Cr)-NiAl [18] Ti(Mo)-TiFe [19, 20] and Nb/Ta refractory high entropy alloy (RM-HEAs), namely $Al_{0.5}NbTa_{0.8}Ti_{1.5}V_{0.2}Zr$ [21]. However, none of these constitute a tungsten-based superalloy with the highest temperature capability.

Designing a tungsten superalloy fundamentally requires selection of a β' reinforcing phase, but no suitable phase has previously been demonstrated. No W binary system provides a direct analogue to that of Ni-Al for Ni-superalloys between fcc-Ni and $L1_2$ Ni_3Al that allow for precipitate reinforcement. Expanding to ternaries, the B2 NiAl could be considered by analogy to Mo-NiAl [16], however, the low solubility for Ni and Al in W, limits such alloys to eutectic microstructures rather than precipitation as in Ni-superalloys, though eutectic themselves show promise. Recent work in the ternary Mo-Ti-Fe system has

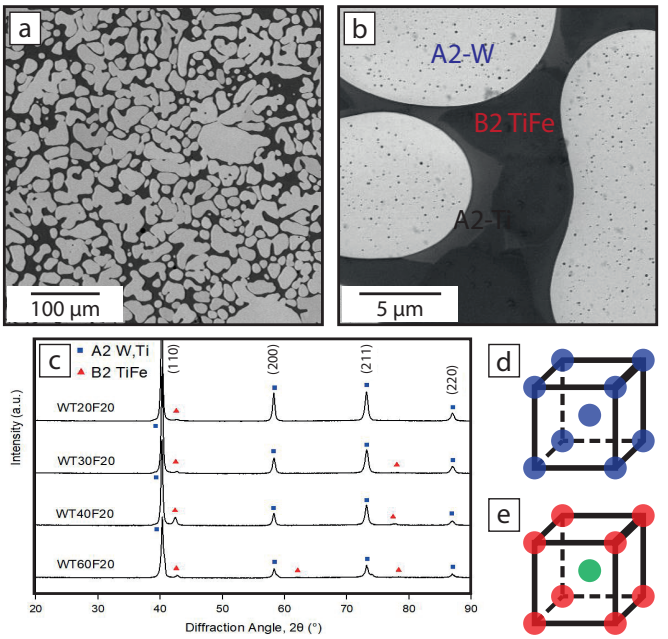

Figure 2: Representative W-Ti-Fe alloy backscattered electron micrographs, for WT30F20 (a) as cast and (b) heat treated at 1250°C, as well as (c) X-ray diffraction for a number of alloys at 1250°C, (e) Bcc A2 unit cell adopted by W and β-Ti, (f) ordered-bcc B2 unit cell adopted by TiFe.

demonstrated the co-existence of B2 TiFe with bcc A2 (Mo,Ti), and further, the possibility of precipitate reinforced β-β' Ti(Mo)-TiFe alloys [19]. This is suggested to be replicated in the W-Ti-Fe system [22] from extrapolation of a thermodynamic model, but has not been experimental demonstrated. It should be noted that nickel based superalloys typically have densities of $8-9\,\mathrm{g\,cm^{-3}}$ that are much lower than that of tungsten $\rho = 19.3\,\mathrm{g\,cm^{-3}}$, which is likely to preclude application of tungsten rich bcc-superalloys for use in rotating parts, however, macro-alloying with Ti may reduce the density to $< 10\,\mathrm{g\,cm^{-3}}$ (see Appendix Table S3).

2. Methods

Ingots ~25 g were prepared by vacuum arc melting of pure (> 99.9%) elements under Ar, by ACI Alloys Inc. The target compositions of W(80-X)%-Ti(X)Fe%-Fe20% (at.%, where X = 60, 40, 30, 20), were targeted to evaluate the extent of the β-β' A2-B2 from Ti to W rich compositions. The density of the W-Ti-Fe alloys were found to be $9.8-15.4\,\mathrm{g\,cm^{-3}}$ with increasing W content (see Appendix Table S3. These were determined by rule of mixtures estimation from the target composition (Table 1), as well as experimental measurement using the Archimedes method. Sections of the ingots were encapsulated within evacuated glass ampoules backfilled with argon and were homogenised at 1250°C for 100 hours and water quenched. The WT60F20 alloy was found to be semi-solid at 1250°C and so a second piece was treated at 1100°C.

Table 1: Alloys compositions measured by 200 x 200 μm EDX area scans in the as-cast condition. Standard deviations give an indication of the variability from location to location due to macro-segregation.

Alloy Designation	Target (at.%)			Measured Composition (at.%)		
W(80-X)-Ti(X)-Fe(20)	W	Ti	Fe	W	Ti	Fe
WT60F20	20	60	20	14.7 ± 2.4	65.7 ± 1.7	19.6 ± 0.7
WT40F20	40	40	20	34.4 ± 0.7	46.1 ± 0.6	19.5 ± 0.1
WT30F20	50	30	20	37.1 ± 2.4	39.4 ± 2.9	23.5 ± 0.6
WT20F20	60	20	20	63.5 ± 1.0	26.2 ± 1.4	10.4 ± 1.8

Scanning electron microcopy (SEM) was performed on a Zeiss Sigma operated at 10 kV for imaging, and on a JEOL 5800 operated at 20 kV for energy-dispersive X-ray spectrometry (EDX). The bulk composition of the alloys were evaluated by averaging five 200 × 200 µm area measurements, at the top, bottom, centre and at either side of a section, see Table 1. Scanning transmission electron microscopy (STEM) was performed using a JEOL 2100F microscope operated at 200 kV. Electron transparent foils were prepared by mechanical thinning 3 mm discs to 150 µm followed by electropolishing using a twin-jet electropolishing unit, with a solution of 10% perchloric acid in methanol at a temperature of −30°C.

Hardness indents using a 1 kg load held for 10 s were made, averaging five measurements, with standard deviations typically < 20 HV. High temperature compression tests were performed in an MRF Inc. vacuum furnace that was maintained with a pressure below 4 x 10^{-4} torr. The furnace was heated with tungsten heating elements and molybdenum heat shields, at a rate of 20°C/min and equilibrated at the set-point for 10 min prior to compression. The temperature was monitored with a W-WRe thermocouple positioned adjacent to the sample. Compression was applied using graphite push rods attached to an Instron universal tester, controlled by an 25 kN Instron 2527 Series load cell. Compression samples were cut into 2x2x3 mm cuboids using electron discharge machining and lightly polished to remove surface damage. The samples were sandwiched between 3 mm SiC spacers to prevent damage to the push rods. Test were carried out at fixed displacement rate of 0.2mm/min, corresponding to a nominal strain rate of $\sim 10^{-3}$ s^{-1}. The yield stress was calculated using the 0.2% offset method. Deflection of the push rods was accounted for using a linear fit to the elastic portion of the load-displacement curve. Oxidation was tested on 2x2x2 mm cuboidal samples in an alumina crucible within a STA 449 F5 Jupiter Thermogravimetric Analyser (TGA). The sample was heated to 1000 °C in Ar and held isothermally. Once the temperature stabilised, air was flowed over the sample at 100 ml/min for 1 h, after which the sample was again purged with Ar and cooled.

3. Results & Discussion

This investigation of the W-Ti-Fe ternary system has three key objectives: (1) To determine experimentally the phase equilibria in the W-Ti-Fe system, (2) To use this new data to instruct a revised thermodynamic assessment to facilitate onward alloy design, (3) To demonstrate W-TiFe A2-B2 β-β' precipitation, and benchmark preliminary properties of tungsten bcc-superalloys against Ni fcc-superalloys.

3.1. W-Ti-Fe System and A2-B2 β-β' Two-phase Determination

To establish the existence of a A2-B2 β-β' W to TiFe two-phase field, a series of alloys were prepared by vacuum arc melting with target compositions W(80-X)-Ti(X)-Fe(20) (X = 20, 30, 40, 60, at.%, abbreviated WT(X)F20 henceforth). In the as-cast condition scanning electron microscopy (SEM) identified dendritic microstructures typical of metal alloys, e.g. Figure 2a. The tungsten rich dendrites were surrounded by inter-dendritic TiFe and/or β-Ti phase, owing to W's high T_m resulting in it being the first to solid to form from the melt.

Annealing heat treatments were applied to determine the stable phases at a given temperature. The alloys were treated at 1250°C for 100 hours, except for the W-lean WT60F20 that was treated at 1100°C to avoid melting. The microstructure of the heat treated alloys resembled their as-cast dendritic microstructure, Figure 2. All alloys exhibited bcc W rich prior-dendrites ~ 10 µm length scale as the majority phase. The inter-dentritic regions contained a darker (lower atomic number, Z) second-phase ~ 5 µm in scale, and in some cases a third phase of similar length-scale. A combination of X-ray diffraction (XRD) and SEM based energy-dispersive X-ray spectroscopy (EDX) were used to identify the crystallography and chemistry of the phases, see Figure 2 and Appendix Figure S1 & Table S2 . XRD determined the alloys exhibited reflections from bcc-related symmetry phases, with at least two phases present in each, which were attributed to a combination of bcc (W or Ti), and ordered-bcc B2 TiFe. The second phase was identified by XRD and EDX to generally be B2 TiFe, which had a low content W of 1-3at%. In some alloys a third phase was also observed with low W content and 30-40at.% Fe content, attributed to be liquid

at 1250°C that solidified on cooling into A2 Ti, by reference to the phase diagram (see Figure 3b). The 1100°C treated WT60F20 alloy was found to comprise stable two-phase bcc W and bcc Ti. The XRD and EDX results are summarised in Appendix Table S2.

3.2. W-Ti-Fe Computational Thermodynamics

Integrated Computational Materials Engineering (ICME) can enable a step-change reduction in the time to develop new materials [23]. However, fundamental to many ICME methods is the availability of computational thermodynamics databases that can accurately predict phases, their compositions toward the ultimate structure/property relationship goals of ICME [24]. The power of computational thermodynamics is that it is very much based on experimental observation that is then used to model simple (unary, binary and ternary) systems that can be combined in multicomponent, multi-system databases. However, this equally means poor availability of prior experimental observations in the simple systems will result in a poor predictive capability of the database. This lack of prior experimental data & tailored database presents a substantial barrier to ICME-based development of bcc-superalloys, which equally extends to refractory high-entropy alloys (RHEAs) and refractory complex concentrated alloys (RCCAs) [25, 26].

As a first fundamental step toward a 'bcc-superalloys' database, a preliminary modelling of the Fe-Ti-W system was undertaken. Existing thermodynamic descriptions for the constituent binary systems, Fe-Ti [27], Fe-W [28], and Ti-W [29], were used as the basis for the work. The extension of the W_6Fe_7 (μ-phase) into the ternary system had been modelled by Qiu & Jin [22] previously and has been adopted here, adapting for the different binary descriptions used. However, it was not possible to use their modelling of the $(Ti,W)Fe_2$ Laves phase as it is not compatible with the model used for the phase in the accepted Fe-Ti binary system, as it is no longer considered a fixed-stoichiometry 'line compound' [22, 27].

Experimental data from the present work and from Qiu & Jin [22] were used in the modelling of the ternary system. The Qiu & Jin [22] data resulted from diffusion couple studies and refer to the isothermal section at 1000°C. Experimental details are sparse and their results were only presented graphically making assessment of the data difficult. The phase diagram data from the present studies refer to isothermal sections at 1100 and 1250°C.

In this preliminary modelling of the system, using Pandat and PanOptimiser, the aim was to see how well combining the accepted binary systems [27–29] and extrapolating into the ternary system agreed with the experimental data listed above (details of the thermodynamic parameters are reported in Appendix Table S4). The initial predictions were encouraging, and by making just a few adjustments to the parameters, a good fit of the calculated phase boundaries to the experimental data was achieved. Figure 3 shows calculated isothermal sections for 1000 and

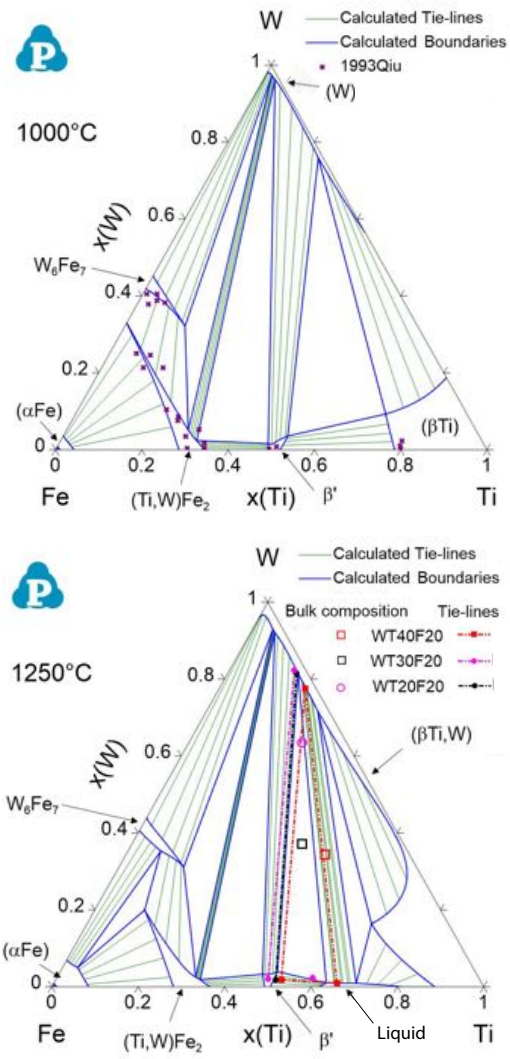

Figure 3: W-Ti-Fe revised thermodynamic assessment: (a) Isothermal section at 1000°C also showing the data from Qiu & Jin [22]. (b) Isothermal section at 1250°C with the present data.

1250°C using the revised set of thermodynamic parameters (see Appendix Figure S2b for 1100°C section). The model essentially contains descriptions for the three binary systems but with two important changes:

(1) The two-sublattice model used for the Laves phase now allows for mixing of all components on both sublattices, which enables its non-stoichiometry to be modelled. However, it was necessary to discourage occupancy of the 'Fe' sublattice by the other two components. The result is a relatively narrow phase field that stretches from the $TiFe_2$ composition on the Fe-Ti system to WFe_2 in the Fe-W binary. This was achieved by ascribing large positive values for the appropriate parameters in the model for the phase. As can be seen in Figure 3, the data from Qiu & Jin [22] agree reasonably well given the experimental uncertainty. It should be noted that the model's fit to the data close to the Fe-Ti binary edge is caused mainly by the location of the phase boundaries in the binary system suggesting this system may need in-depth study.

(2) Most problematic was fitting to the experimental data for the (W)-bcc solid solution determined in this work. This is of critical importance toward a bcc-superalloy database as the (W)-bcc change in solubility for Fe and Ti with temperature provides the fundamental driving force for precipitation of B2 TiFe from within a (W) matrix. The (W) phase boundary calculated using the binary descriptions as taken from the literature significantly underestimated the Fe solubility within (W)-bcc. In order for the calculated curve to agree with the ternary experimental data, it was necessary to reconsider the binary dataset for the Fe-W system, shifting the W-rich solvus to higher Fe contents (see Appendix Figure S2a). However, adjusting the binary solvus really requires a full reoptimisation of the binary system, which we will present in a future publication.

Ultimately the computational thermodynamic assessment of the W-Ti-Fe system shows good fit to the available data, Figure 3. This assessment establishes greatly improved predictive capability for further alloy development within the system. Further, it provides a foundation from which a wider 'bcc-superalloys' database can be established, enabling ICME methods to be exploited to accelerate the time to market of these next-generation high temperature materials.

3.3. Bcc W Superalloy: Demonstration & Properties

Whilst stable coexistence of two-phase bcc W and ordered-bcc B2 TiFe was demonstrated and modelled in the W-Ti-Fe system (Figure 3), this does not necessarily enable precipitate strengthening analogous to nickel superalloys where reinforcement is introduced by a secondary 'ageing' heat treatment. To test whether a driving force for β' precipitation exists owing to change in solute solubility with temperature, the solution heat treated alloys were aged at 750°C for 80 h, following [19]. It was found that a nano-scale precipitate phase in fact formed within the bcc W dendrites during heat treatment at 1250°C (Figure 2b), which did not perceptibly change on ageing at 750°C (Appendix Figure S3b), noting also that no such nano-precipitates were observable in the as cast condition (Appendix Figure S3a). Given that only bcc and B2 reflections were observed by XRD, it was considered this nano-scale phase was likely to be TiFe formed by precipitation.

Transmission electron microscopy (TEM) and scanning TEM (STEM) were employed to resolve the nature of the nano-scale features, Figure 4. Composition mapping by STEM-EDX identified a W rich matrix with the ~ 50 nm precipitates found to be rich in Ti and Fe, consistent with the TiFe intermetallic compound. This was supported by STEM-EDX point scans that indicated a composition of ~54Ti-40Fe-6W (at.%), suggesting some off-stoichiometric solubility. In HAADF Figure 4b a larger black region can be seen that is not enriched in Fe and Ti indicating it is most likely a hole where a TiFe particle has fallen out during electropolishing leaving thinned W matrix.

Selected area diffraction pattern (SADP) analysis was performed to confirm the crystallography of the precipitates and to determine their orientation relationship with the surrounding matrix. Dominant reflections were readily observed from the bcc W matrix, [110] zone axis, Figure 4e. However, by careful overexposure and summing of frames, {001} reflections indicative of ordered-bcc B2 TiFe were revealed, Figure 4f inset. The TiFe reflections appear weak, compared to those of W, due to a combination of: differences in scattering factor, structure factor and volume fraction; as was similarly observed for XRD reflections (Figure 2c). Whilst single diffraction spots are typical, in Figure 4e multiple spots can be observed around the 001 superlattice reflections. This phenomena is termed 'double diffraction' whereby a diffraction beam from within one phase is diffracted again within an adjacent second-phase, due to the precipitates being smaller than the TEM foil thickness [30]. Consideration of the crystallography between the bcc matrix and B2 precipitate reflections found

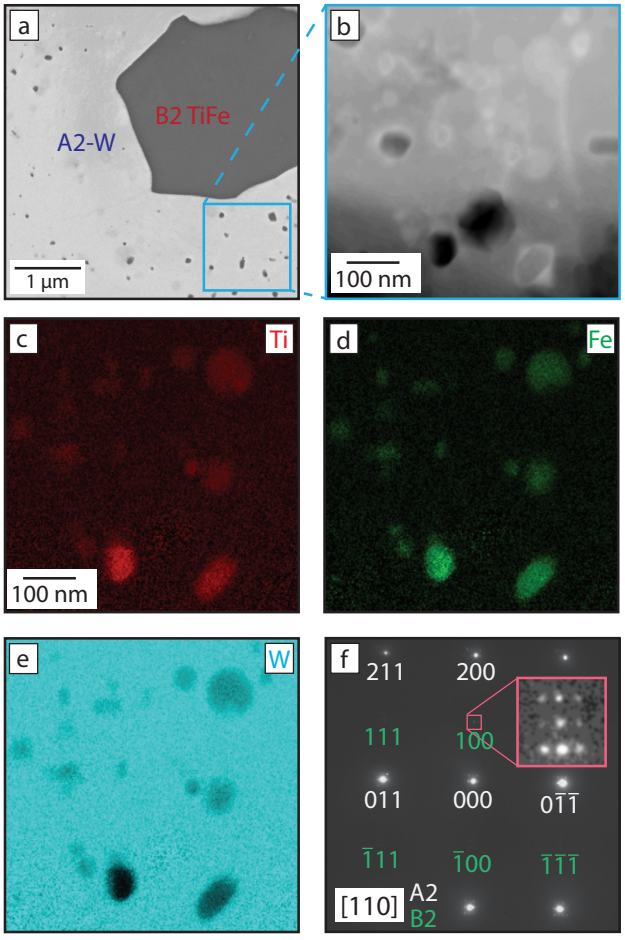

Figure 4: WT30F20 alloy heat treated 1250°C + 750°C 80 h, (a) SEM BSE, (b) STEM-HAADF, and elemental maps of (c) Ti, (d) Fe and (e) W, and (f) Bcc+B2 selected area diffraction pattern (SADP) using a 100 nm aperture showing A2 parent reflections (white) and B2 superlattice reflections (green) where $(002)_{bcc} \backslash\backslash (002)_{B2}$, with (f-inset) showing an expansion with heightened contrast of the $(001)_{B2}$ superlattice reflection, with double diffraction.

them to obey a 'cube-cube' orientation relationship (OR), where $(001)_{bcc}\backslash\backslash(001)_{B2}$. This manner of OR is directly comparable with nickel superalloys that follow $(001)_{\gamma}\backslash\backslash(001)_{\gamma'}$. Ni superalloys have low lattice misfits of +2 to -2% that are known to strongly influence strength, creep and coarsening characteristics [2]. However, the WT30F20 alloy exhibited a markedly larger misfit of δa ~5%, calculated from XRD following $\delta a = \delta a_{B2} - a_{A2}/a_{A2}$ [17]. Onward alloy design will need to reduce the lattice misfit perhaps through quaternary or quinary alloying. Such alloy development will be greatly accelerated by the exploitation of a bcc superalloy thermodynamic database and ICME methods.

Mechanical property determination is critical to evaluate the usefulness of the new microstructure concept β-β' A2-W + TiFe. Here first screening was made by hardness. The alloys exhibited very highness of 550 to 650 HV (5-6 GPa) across the compositions and heat treatments used, Figure 5. Given the high starting hardness no discernible age hardening was associated with the ageing and precipitate formation (Appendix Figure S4). To gain preliminary understanding as to the elevated temperature properties of the alloys testing was performed at 500 and 1000°C by hot-compression under vacuum, Figure 5. This found the alloy maintained high strength ~ 500 MPa at 1000°C, which is higher than tungsten benchmarks for W hardness [31] and strength as rolled/recrystallised [32], and further, offers a significant improvement over nickel-based superalloys Inconel 718 [33] & Haynes 230 [34]. The oxidation behaviour of the WTi30Fe20 alloy at 1000 °C (shown in Appendix Figure S5) found the oxidation mass gain kinetics were initially parabolic, but became linear after 20 mins, where the linear kinetic constant approached 12 µg/cm^2-s. This is typical of tungsten oxidation, e.g. under similar conditions linear rate constants in the range $10 - 30$ µg/cm^2-s have been reported [35–38].

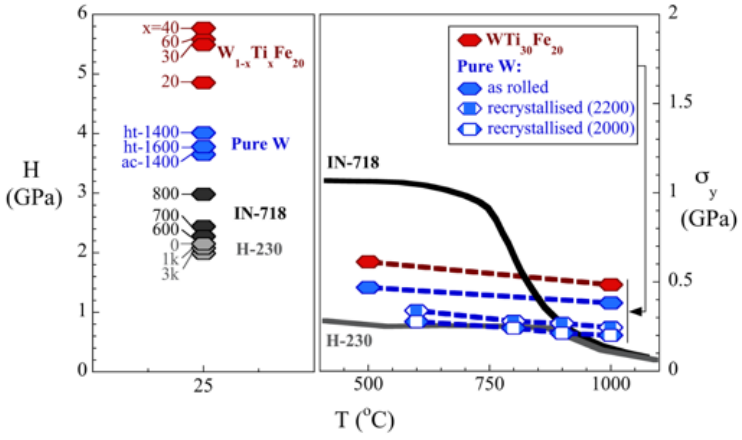

Figure 5: Hardness H (GPa) and high temperature compression strength (GPa, axis scaled to 1/3 H) of the tungsten superalloys, against W hardness [31] & strength as rolled/recrystallised [32], as well as nickel-based superalloys IN718 [33] and H230 [34].

4. Conclusions

In Conclusion, the W-Fe-Ti system demonstrates A2-B2 β-β' microstructures that offer a route to a new class of 'tungsten-based bcc-superalloys'. This has been achieved through determination of the phase equilibria, demonstrating the co-existence of β-β' (W,Ti)-TiFe phases. The new data has been integrated into a thermodynamic model to facilitate the onward computational engineering (ICME) of bcc superalloys. Characterisation revealed for the first time that β' B2 TiFe intermetallic precipitates can be produced from within a W-rich matrix. These precipitates offer new prospects for the design of alloys for high temperature applications, with the alloys demonstrating exceptional strength at high temperature of 1000°C.

Acknowledgements

This work was supported by: UKRI Future Leaders Fellowship (AJK), Royal Academy of Engineering Research Fellowship (AJK), EUROfusion Researcher Grant Fellowship (AJK), and Imperial College Research Fellowship (SHB).

References

[1] M. J. Donachie and S. J. Donachie, *Superalloys: A Technical Guide*. ASM International, second ed., 2002.

[2] R. C. Reed, *The Superalloys: Fundamentals and Applications*. Cambridge University Press, 2006.

[3] J. Sato, T. Omori, K. Oikawa, I. Ohnuma, R. Kainuma, and K. Ishida, "Cobalt-Base High-Temperature Alloys," *Science*, vol. 312, pp. 90–91, 2006.

[4] L. A. Cornish, B. Fischer, and R. Völkl, "Development of Platinum-Group-Metal Superalloys for High-Temperature Use," *MRS Bulletin*, vol. 28, no. 9, pp. 632–638, 2003.

[5] Y. Yamabe, Y. Koizumi, H. Murakami, Y. Ro, T. Maruko, and H. Harada, "Development of Ir-base refractory superalloys," *Scripta Materialia*, vol. 35, no. 2, pp. 211–215, 1996.

[6] C. Ren, Z. F. Fang, M. Koopman, B. Butler, J. Paramore, and S. Middlemas, "Methods for improving ductility of tungsten - A review," *International Journal of Refractory Metals & Hard Materials*, vol. 75, pp. 170–183, 2018.

[7] G. Schmidt, "Propulsion research and technology at NASA Marshall Space Flight Center," *ASEE Joint Propulsion Conference and Exhibit*, 1998.

[8] D. Snow, "The recrystallization of commercially pure and doped tungsten wire drawn to high strain," *METALLURGICAL TRANSACTIONS A*, vol. 10A, pp. 815–821, 1979.

[9] C. Bonnekoh, A. Hoffmann, and J. Reiser, "The brittle-to-ductile transition in cold rolled tungsten_ On the decrease of the brittle-to-ductile transition by 600K to -65°C," *International Journal of Refractory Metals & Hard Materials*, vol. 71, pp. 181–189, 2018.

[10] P. L. Raffo, "Yielding and fracture in tungsten and tungsten-rhenium alloys," *Journal of the Less Common Metals*, vol. 17, no. 2, pp. 133–149, 1969.

[11] A.ZUpadhyaya, "Processing strategy for consolidating tungsten heavy alloys for ordnance applications," *Materials Chemistry and Physics*, vol. 67, pp. 101–110, 2001.

[12] R. Neu, H. Maier, M. Balden, S. Elgeti, H. Gietl, H. Greuner, A. Herrmann, A. Houben, V. Rohde, B. Sieglin, "Investigations on tungsten heavy alloys for use as plasma facing material," *Fusion Engineering and Design*, vol. 124, pp 450–454, 2017.

[13] K.M. Ostolaza Zamora, J.G. Sevillano, M. Fuentes Pérez, "Fracture toughness of W heavy metal alloys," *Materials Science and Engineering: A*, vol. 157, pp 151–160, 1992.

[14] U. Ravi Kiran, A. Panchal, M. Sankaranarayana, G. Nageswara Rao, and T. Nandy, "Effect of alloying addition and microstructural parameters on mechanical properties of 93% tungsten heavy alloys," *Materials Science & Engineering A*, vol. 640, pp. 82–90, 2015.

[15] J. Iv, D. J. Edwards, C. H. Henager Jr., W. Setyawan, J. Wang, and M. Murayama, "Characterization of Ductile Phase Toughening Mechanisms in a Hot-Rolled Tungsten Heavy Alloy," *Acta Materialia*, vol. 204, pp. 1–11, 2021.

[16] H. Bei and E. George, "Microstructures and mechanical properties of a directionally solidified NiAl–Mo eutectic alloy," *Acta Materialia*, vol. 53, no. 1, pp. 69–77, 2005.

[17] G. Ghosh and G. B. Olson, "Integrated design of Nb-based superalloys: Ab initio calculations, computational thermodynamics and kinetics, and experimental results," *Acta Materialia*, vol. 55, pp. 3281–3303, 2007.

[18] C. Stallybrass, A. Schneider, and G. Sauthoff, "The strengthening effect of (Ni,Fe)Al precipitates on the mechanical properties at high temperatures of ferritic Fe–Al–Ni–Cr alloys," *Intermetallics*, vol. 13, pp. 1263–1268, 2005.

[19] A. J. Knowles, T. Jun, A. Bhowmik, N. G. Jones, T. B. Britton, F. Giuliani, H. J. Stone, and D. Dye, "A new beta titanium alloy system reinforced with superlattice intermetallic precipitates," *Scripta Materialia*, vol. 139, pp. 71–75, 2017.

[20] E. Calvert, A. Knowles, J. Pope, D. Dye, and M. Jackson, "Novel high strength titanium-titanium composites produced using field-assisted sintering technology (FAST)," *Scripta Materialia*, vol. 159, pp. 51–57, 2019.

[21] V. Soni, O. N. Senkov, B. Gwalani, D. B. Miracle, and R. Banerjee, "Microstructural Design for Improving Ductility of An Initially Brittle Refractory High Entropy Alloy," *Scientific Reports*, vol. 8, no. 8816, pp. 1–10, 2018.

[22] C. Qiu and Z. Jin, "An experimental study and themodynamic evaluation of the Fe-Ti-W system at 1000°C," *Scripta Metallurgica et Materialia*, vol. 28, pp. 85–90, 1993.

[23] M. F. Horstemeyer, *Integrated Computational Materials Engineering (ICME) for Metals: Using Multiscale Modeling to Invigorate Engineering Design with Science*. Wiley, 2012.

[24] H.-L. Lukas, S. G. Fries, and B. Sundman, *Computational Thermodynamics: The Calphad Method*. Cambridge University Press, 2007.

[25] S. Wei, S. J. Kim, J. Kang, Y. Zhang, Y. Zhang, T. Furuhara, E. S. Park, and C. C. Tasan, "Natural-mixing guided design of refractory high-entropy alloys with as-cast tensile ductility," *Nature Materials*, vol. 19, pp. 1175–1181, Nov. 2020.

[26] O. N. Senkov, D. B. Miracle, K. J. Chaput, and J.-P. Couzinie, "Development and exploration of refractory high entropy alloys—A review," *Journal of Materials Research*, vol. 33, pp. 3092–3128, Oct. 2018.

[27] H. Bo, J. Wang, L. Duarte, C. Leinenbach, L.-b. Liu, H.-s. Liu, and Z.-p. Jin, "Thermodynamic re-assessment of Fe–Ti binary system," *Transactions of Nonferrous Metals Society of China*, vol. 22, no. 9, pp. 2204–2211, 2012.

[28] A. Jacob, C. Schmetterer, L. Singheiser, A. Gray-Weale, B. Hallstedt, and A. Watson, "Modeling of Fe–W phase diagram using first principles and phonons calculations," *Calphad*, vol. 50, pp. 92–104, 2015.

[29] N. Saunders, "COST507 final report: COST507 Thermochemical database for light metal alloys," tech. rep., 1998.

[30] S. B. Williams and C. B. Carter, *Transmission Electron Microscopy: A Textbook for Materials Science*. Springer, 2009.

[31] M. Fukuda, T. Tanno, S. Nogami, and A. Hasegawa, "Effects of Re Content and Fabrication Process on Microstructural Changes and Hardening in Neutron Irradiated Tungsten," *Materials Transactions - The Japan Institute of Metals*, vol. 53, no. 12, pp. 2145–2150, 2012.

[32] T. Zhang and S. Guiming, *The High Temperature Compressive Behaivor of ZrCp/W Composites and the Strengthening Mechanisms*. PhD Thesis, Harbin Institute of Technology, Harbin, China, 2008.

[33] "Inconel® Alloy 718 Datasheet," Tech. Rep. SMC-045, Special Metals, 2007.

[34] "Haynes® 230® Alloy Datasheet," Tech. Rep. H-3000 M, Haynes International, 2018.

[35] S.A. Humphry-Baker, W.E. Lee, "Tungsten carbide is more oxidation resistant than tungsten when processed to full density," *Scripta Materialia*, vol. 116, pp 67–70, 2016.

[36] P.E. Blackburn, K.F. Andrew, E.A. Gulbransen, F.A. Brassart, "Oxidation of Tungsten and Tungsten Based Alloys," *WESTINGHOUSE ELECTRIC CORP PITTSBURGH PA*, 1961.

[37] F. Koch, H. Bolt, "Self passivating W-based alloys as plasma facing material for nuclear fusion," *Phys. Scr.*, vol 100, 2007.

[38] W.W. Webb, J.T. Norton, C. Wagner, "Oxidation of Tungsten," *J. Electrochem. Soc.*, vol. 103, 1956.

[39] A. Dinsdale, A. Watson, A. Kroupa, J. Vrestal, A. Zemanova, J. Vizdal *COST531, Lead Free Solders Volume 1: Atlas of phase Diagrams of Lead-Free Soldering*, 2008.

[40] Y.M. Muggianu, M. Gambino, J.P. Bros, "Enthalpies de formation des alliages liquides bismuth-etain-gallium a 723 K" *J. Chim. Phys.*, vol. 72, pp 83-88, 1975.

[41] O. Redlich, A. Kister, "Algebraic Representation of Thermodynamic Properties and the Classification of Solutions" *Indust. Eng. Chem.*, vol. 40, pp 345–348, 1948.

[42] J.O. Andersson, A. Fernandez Guillermet, M. Hillert, B. Jansson, B. Sundman, "A compound-energy model of ordering in a phase with sites of different coordination numbers" *Acta Met.* vol. 34, pp. 437-445, 1986.

[43] J. Lacaze, B. Sundman, "Assessment of the Fe-C-Si System" *Met. Trans. A*, vol. 22A, pp 2211-2223, 1991.

[44] B. Hallstedt, "Thermodynamic database for high- and medium-manganese steels" *4th International Conference on Medium and High Manganese Steels (HMnS2019) Proceedings*, W. Bleck, D. Raabe (Eds.), pp 201–204, 2019.
[45] A. Antoni-Zdziobek, T. Commeau and J.M. Joubert, *Metall. Mater. Trans. A*, vol. 44, pp 2996-3003, 2013.
[46] A.T. Dinsdale, "SGTE Pure Element Transition Data" *Calphad*, vol. 15, pp 317-425, 1991.
[47] M.H.F. Sluiter "Ab initio lattice stabilities of some elemental complex structures" *Calphad*, vol. 30, pp 357-66, 2006.

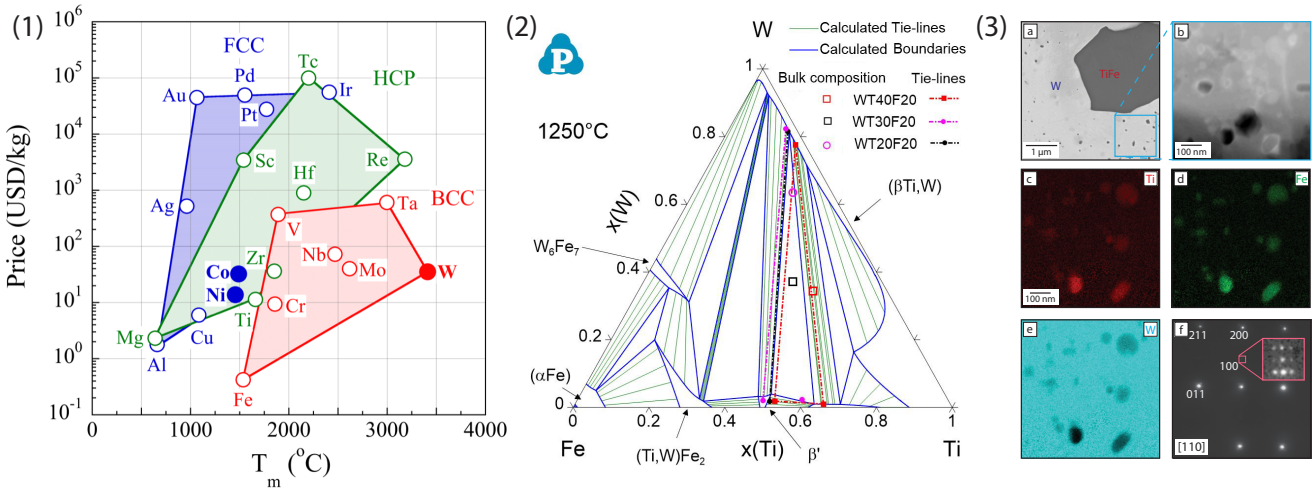

Figure Graphical Abstract 1: Tungsten-based bcc-superalloy (1) Motivation by price vs Melting point T_m, (2) Modelling by CALPHAD, (3) Demonstration, TEM characterisation of TiFe precipitates.

Appendix

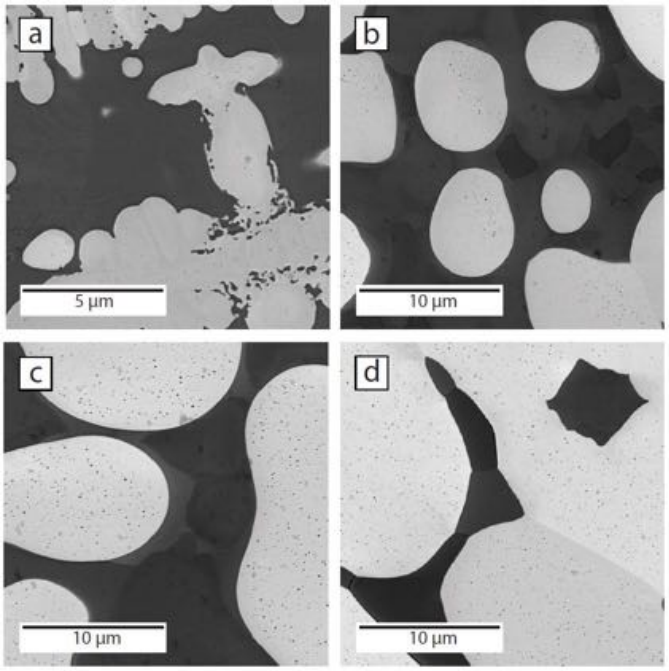

Figure S1: W-Ti-Fe alloys following heat treatment, (a) WT60F20 at 1100°C, and the rest at 1250°C (b) WT40F20, (c) WT30F20 and (d) WT20F20.

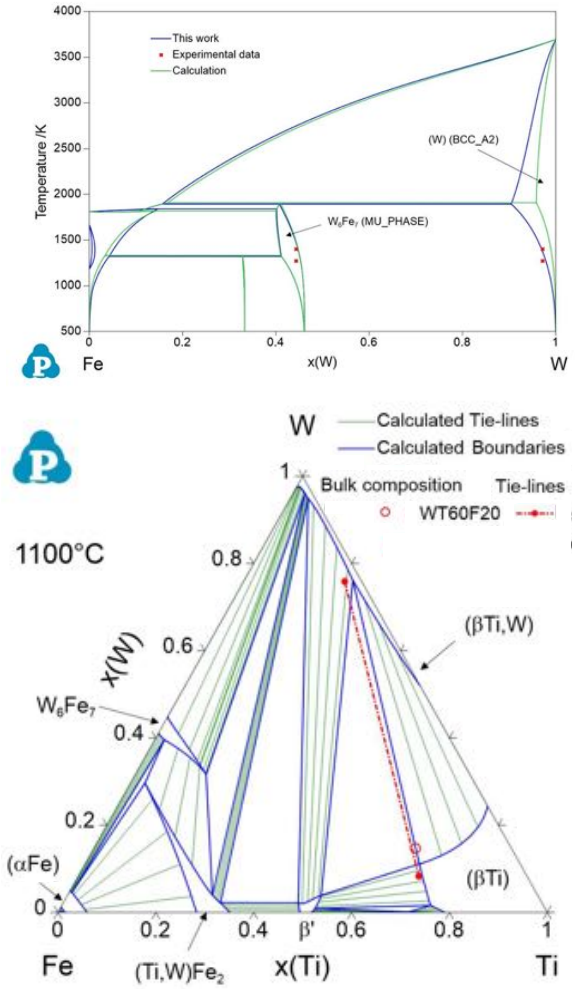

Figure S2: W-Ti-Fe revised thermodynamic assessment, (a) Fe-W binary [28] with modification for W(Fe) solubility, (b) Isothermal section at 1100°C with the present data.

Supplementary Table S1. Price and melting point data for various metal elements plotted in Fig. 1.

Symbol	Structure	T_m (°C)	Price (USD/kg)	Notes
Al	FCC	660	1.79[1]	High-grade primary Al, London Metal Exchange (LME) warehouse.
Co	FCC	1495	32.8[1]	Spot price. Min. 99.8% pure. LME warehouse.
Ni	FCC	1453	13.9[1]	Primary Ni. Spot price. Min. 99.8% pure. LME warehouse.
Cu	FCC	1083	6[1]	Spot price. Grade A.[30] LME warehouse.
Pd	FCC	1552	49500[1]	See also: Palladium as an investment
Ag	FCC	962	521[1]	See also: Silver as an investment
Ir	FCC	2410	56000[2]	99.95% pure.
Pt	FCC	1772	27800[1]	See also: Platinum as an investment
Au	FCC	1064	44800[1]	See also: Gold as an investment
V	BCC	1890	371[2]	Min. 99.5% pure.
Cr	BCC	1857	9.4[1]	Min. 99.2% pure.
Fe	BCC	1535	0.424[2]	L8-10 pig iron. At Tangshan, China.
Nb	BCC	2468	73[2]	Min. 99.9% pure.
Mo	BCC	2617	40.1[1]	Min. 99.95% pure.
Ta	BCC	2996	605[3]	Min. 99.95% pure. Ex Works China.
W	BCC	3410	35.3[1]	Powder, particle size 2–10 μm, 99.7% pure. Free on Board China.
Mg	HCP	639	2.32[1]	Min 99.9% pure.
Sc	HCP	1539	3460[3]	Min. 99.99% pure.
Ti	HCP	1660	11.4[2]	Min. 99.6% pure titanium sponge.
Zr	HCP	1852	36.4[2]	Zirconium sponge, min. 99% pure.
Tc	HCP	2200	100,000[4]	
Hf	HCP	2150	900[5]	Unwrought hafnium.
Re	HCP	3180	3600[2]	99.99% pure.

[1] "Preismonitor" from Destatis Statistics: https://www.destatis.de/EN/Home/_node.html (accessed May 2020)

[2] Shanghai Metals Market: https://www.metal.com/ (accessed May 2020)

[3] Institute of Rare Earths and Metals: https://en.institut-seltene-erden.de/ (accessed May 2020)

[4] Handbook of Chemistry and Physics, CRC Press (2004), 84th edition, editor: DR Lide

[5] US Geological Survey: National Minerals Information Centre https://www.usgs.gov/ (accessed May 2020)

Table S2: Phases indicated by XRD and compositions measured by SEM-EDX.

Alloy & treatment	Phase identified	W (at.%)	Ti (at.%)	Fe (at.%)
WT60F20	A2 W Dendrite	75.9 ± 1.5	20.6 ± 1.3	3.5 ± 0.4
@ 1100°C	A2 Ti (inter-dendritic)	8.3 ± 0.8	69.6 ± 0.8	22.1 ± 0.4
WT40F20	A2 W Dendrite	77.5 ± 1.4	19.9 ± 0.8	2.6 ± 0.7
@ 1250°C	B2 TiFe (inter-dendritic)	1.9 ± 0.1	52.2 ± 0.4	45.9 ± 0.3
	A2 Ti (inter-dendritic)	1.0 ± 0.2	65.5 ± 1.6	33.5 ± 1.6
WT30F20	A2 W Dendrite	81.6 ± 1.2	15.9 ± 0.6	2.6 ± 0.8
@ 1250°C	B2 TiFe (inter-dendritic)	1.8 ± 0.2	51.0 ± 0.7	47.3 ± 0.6
WT20F20	A2 W Dendrite	82.3 ± 2.4	15.0 ± 1.4	2.7 ± 1.0
@ 1250°C	B2 TiFe (inter-dendritic)	2.1 ± 0.3	49.1 ± 0.9	48.9 ± 0.6
	A2 Ti (inter-dendritic)	2.3 ± 0.1	59.3 ± 0.4	38.5 ± 0.4

Table S3: Alloys' Density: Estimated from target/SEM-EDX compositions, Table 1, and Measured by Archimedes' Method

Alloy	Density estimated from Target compositions	Density Measurement by Archimedes' Method
WT60F20	8.1	9.8
WT40F20	11.1	11.0
WT30F20	12.6	12.7
WT20F20	14.1	15.4

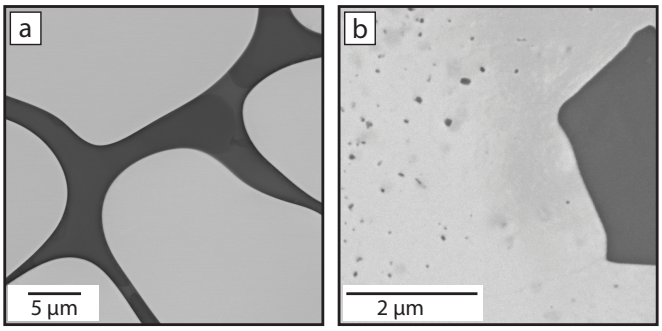

Figure S3: SEM BSE micrograph of alloy WT30F20, (a) as cast, and (b) heat treated at 1250°C + 750°C with inset showing a bcc-W + B2-TiFe precipitates region similar to that evaluated by TEM in Figure 4.

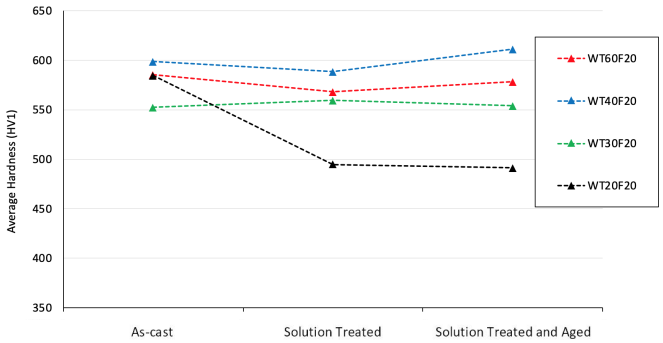

Figure S4: W-Ti-Fe alloys hardness (GPa) vs condition.

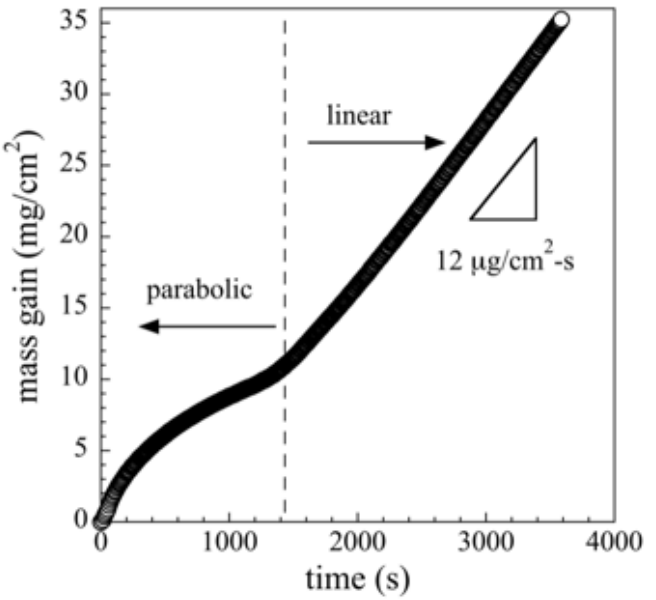

Figure S5: WT30F20 aged alloy oxidation at 1000 °C mass gain vs time.

Appendix: Thermodynamic modelling

As indicated in the text, a preliminary modelling of the Fe-Ti-W system was undertaken to complement the experimental programme. Techniques used have been described elsewhere [24] but involve using experimental observations to fix parameters of models that describe the Gibbs energies of the phases in the system.

The Gibbs energy of a substitutional solution φ is given by a number of Gibbs energy contributions [39]:

$$G_m^{\varphi} = G_{ref}^{\varphi} + G_{id}^{\varphi} + G_E^{\varphi} + G_{mag}^{\varphi} + G_P^{\varphi} + \cdots$$

where G_{ref}^{φ} is the weighted sum of the Gibbs energies of the system constituents, *i*, in phase φ relative to the chosen reference state of the dataset,

$$G_{ref}^{\varphi} = \sum_{i=1}^{n} x_i \cdot {}^{\mathrm{O}}G_i^{\varphi}$$

The ideal mixing contribution to the Gibbs energy is given by:

$$G_{id}^{\varphi} = \mathrm{R}T \sum_{i=1}^{n} x_i \cdot \ln(x_i),\ x = 1, \ldots m$$

The deviation from ideality is expressed by the Muggianu extension of the Redlich-Kister formulism [40,41]:

$$G_E^{\varphi} = \sum_{\substack{i,j=1,\\ i\neq j}}^{n} x_i x_j \sum_{z=0}^{m} {}^{z}L\left(x_i - x_j\right)^z + \sum_{\substack{i,j,k=1,\\ i\neq j\neq k}}^{n} x_i x_j x_k \, {}^{z}L_{ijk}\ z = 0, \ldots, m$$

where the terms *L* are adjustable model parameters. In addition, the *temperature* dependence of the Gibbs energy (and also the *L* parameters) is given by

$$G(T) = a + bT + cT\ln(T) + dT^2 + eT^3 + fT^{-1}$$

where *a-f* are adjustable coefficients.

More complex phases such as the (Ti,W)Fe_2 Laves and W_6Fe_7 mu-phase employ the *Compound Energy Formalism* [42] where aspects of the crystal structure of the phase is incorporated into the model. The crystal structure can be considered of having a set of sublattices, *l*, showing some degree of preferential occupancy by one or more of the constituents. Then:

$$G_{ref}^{\varphi} = \sum y_i^s \cdot y_j^t \cdots y_k^u \ {}^{\mathrm{O}}G_{(i:j:\cdots:k)}, i, j, k = 1, \ldots, n, s, t, u = 1, \ldots., l$$

where the *y* terms are the site fractions of constituent *i-k* on sublattice *s-u*. The *G* terms of the equation are the 'end-members' or 'virtual compounds' of the phase. The ideal mixing contribution to the Gibbs energy is given as:

$$G_{id}^{\varphi} = \sum_{p=1}^{l} f_p \cdot \sum_{i=1}^{m} y_i^p \cdot \ln\left(y_i^p\right)$$

where f_p is the stoichiometry of sublattice *p*. The excess Gibbs energy is given by:

$$G_E^{\varphi} = \sum y_i^p \cdot y_j^p \cdot y_k^q \, L_{(i,j:k)}$$

where

$$L_{(i,j:k)} = \sum_z {}^z L_{(i,j:k)} \cdot \left(y_i^p - y_j^q\right)^z$$

Here, the *L* parameter describes the interaction of constituents *I* and *j* on the first sublattice with the second completely occupied by constituent *k*. In addition to describing the thermodynamic properties of intermetallic phases, this expression can be combined with that for substitutional solutions in order to model order/disorder transitions as in the case of BCC_A2/BCC_B2.

In this work, the focus for the preliminary assessment of the ternary system was the (Ti,W)Fe_2 Laves phase, the β, β' and (W) phases. The last three phases, being all BCC are treated with the same description but with the inclusion of a contribution describing chemical ordering [43].

Binary datasets were taken from the literature [27-29] with amendments to the data for the Fe-Ti system from [44]. This ensured compatibility between the Fe-Ti and Fe-W systems with respect to the unary data for the (Ti,W)Fe_2 phase.

The experimental ternary data for 1250°C in the W corner of the phase diagram are very close to the Ti-W binary edge. The location of the (W) solvus in the Fe-W binary system has an effect on how it extends into the ternary system. Looking at the assessed Fe-W phase diagram it can be seen that the solvus doesn't fit the experimental data from [45] very well. Remodelling the (W) phase in the binary system to improve the fit helped to fit the phase boundary in the ternary system to the experimental data. Figure S2a shows the Fe-W phase diagram with the adjusted (W) solvus, but it is clear that more work is required to improves the diagram at the Fe end. This is the subject of ongoing work.

In addition to the remodelling of the Fe-W (W) phase (BCC_A2), ternary parameters were added to reduce the extent of the β'-phase (BCC_B2) into the ternary system from the Fe-Ti binary edge.

The parameters adjusted during this work are given in Table S4

Table S4 – Parameters used in the present work. Data for the elements are taken from [46]

Phase	Model	Parameter	Value	Source
Liquid	(Fe,Ti,W)	${}^0L$ (Fe,Ti)	-74300+17.839*T	[27]
		${}^1L$ (Fe,Ti)	8299.849-6.101*T	[27]
		${}^0L$ (Fe,W)	-25460.9+14.97	[28]
		${}^1L$ (Fe,W)	1743.7	[28]
		${}^2L$ (Fe,W)	4633.3	[28]
		${}^0L$ (Ti,W)	28392	[29]
		${}^1L$ (Fe,W)	-4282	[29]
FCC_A1[a]	$(Fe,Ti,W)_1(Va)_1$	${}^0L$ (Fe,Ti)(Va)	-52149.856+9.265	[27]
		${}^1L$ (Fe,Ti)(Va)	4755.900-4.982*T	[27]
		${}^2L$ (Fe,Ti)(Va)	29205.228-11.046*T	[27]
		${}^0L$ (Fe,W)(Va)	+980.9+10*T	[28]
		${}^0L$ (Ti,W)(Va)	33825	[29]
BCC_A2[a] ((αFe)/(W)/ (βTi,W))	$(Fe,Ti,W)_1(Va)_3$	${}^0L$ (Fe,Ti)(Va)	-9241.924+25.246*T +0.0001*T**2 +120000*T**(-1)	[27]
		${}^1L$ (Fe,Ti)(Va)	5018.986-4.992*T	[27]
		${}^2L$ (Fe,Ti)(Va)	23028.241-13.110*T	[27]
		${}^0L$ (Fe,W)(Va)	+8707.65+15.84*T	[28]
		${}^1L$ (Fe,W)(Va)	-4989.8	This work
		${}^2L$ (Fe,W)(Va)	-334.715	This work
		${}^0L$ (Ti,W)(Va)	3957+13.033*T	[29]
		${}^1L$ (Ti,W)(Va)	10640-4.464*T	[29]

		${}^{2}L$ (Fe,Ti,W)(Va)	-40000	This work
BCC_B2[b] (β')	$(Fe,Ti,W)_{0.5}$ $(Fe,Ti,W)_{0.5}(Va)_3$	*G*(Fe)(Ti)(Va)	-30028.003+4.495*T	[27]
		G(Ti)(Fe)(Va)	-30028.003+4.495*T	[27]
		G(Ti)(W)(Va)	0	[27]
		G(W)(Ti)(Va)	0	[27]
		${}^{1}L$ (Fe,Ti)(Ti)(Va)	11000	[27]
		${}^{1}L$ (Ti)(Fe,Ti)(Va)	11000	[27]
		${}^{1}L$ (Fe,Ti)(Fe)(Va)	-5001.5	[27]
		${}^{1}L$ (Fe)(Fe,Ti)(Va)	-5001.5	[27]
		${}^{0}L$ (Ti)(Ti,W)(Va)	0	[29]
		${}^{0}L$ (W)(Ti,W)(Va)	0	[29]
		${}^{0}L$ (Ti,W)(Ti)(Va)	0	[29]
		${}^{0}L$ (Ti,W)(W)(Va)	0	[29]
HCP_A3 (αTi)	$(Fe,Ti,W)_1(Va)_{0.5}$	${}^{0}L$ (Fe,Ti)(Va)	-25000+35.004*T	[27]
		${}^{0}L$ (Fe,W)(Va)	25977-3.36*T	[28]
		${}^{1}L$ (Fe,W)(Va)	-7258.6	[28]
		${}^{0}L$ (Ti,W)(Va)	35774	[29]
μ-phase (W_6Fe_7)	$(Fe,W)_1(Ti,W)_4(Fe,Ti,W)_2(Fe,W)_6$	*G*(Fe)(Ti)(Fe)(Fe)	7**G*(FCC,Fe)+4**G*(BCC,Ti)+ 2**G*HSER,(Fe)[c]	This work
		G(Fe)(Ti)(Ti)(Fe)	7**G*(FCC,Fe)+6**G*(BCC,Ti)	[22]
		G(Fe)(W)(Ti)(Fe)	7**G*(FCC,Fe)+2*(BCC,Ti)+ 4**G*HSER,(W)-170540	[22]
		G(Fe)(Ti)(W)(Fe)	7**G*(FCC,Fe)+4*(BCC,Ti)+ 2**G*HSER,(W)	[22]
		G(W)(W)(W)(W)	13**G*HSER,(W)+469300	[47]
		G(Fe)(W)(Fe)(Fe)	9**G*HSER,(Fe)+4**G*HSER,(W) -76329+39.68*T	[28]
		G(Fe)(W)(Fe)(W)	430118+1680.9*T -321.69*T*Ln(T) -8.17E-04*T**2 +510840.6*T**(-1)	[28]
		G(Fe)(W)(W)(Fe)	-141384.5+1685*T -315.63*T*Ln(T) -0.0051419*T**2 +694229.8*T**(-1) -1.3199E-06*T**3	[28]
		G(Fe)(W)(W)(W)	*G*HSER,(Fe)+12**G*HSER,(W) +375549	[28]
		G(W)(W)(Fe)(Fe)	8**G*HSER,(Fe)+5**G*HSER,(W) +78213	[28]
		G(W)(W)(Fe)(W)	484185+1675.9*T -322*T*Ln(T)-7.198E-04*T**2 +491025.1*T**(-1)	[28]
		G(W)(W)(W)(Fe)	-111740.6+1697.2*T -314.1*T*Ln(T) -0.01214*T**2 +647792.1*T**(-1)	[28]
Laves-phase ($(Ti,W)Fe_2$)	$(FE,TI,W)_2(FE,TI,W)_1$	*G*(Fe)(Fe)	3**G*HSER,(Fe)+44130	[28]
		G(Ti)(Ti)	3**G*HSER,(Ti)+45000	[27]
		G(W)(W)	3**G*HSER,(W)+ 131400	[47]
		G(Fe)(Ti)	-85500+410.041*T -73.553*T*Ln(T) -0.01017*T**2 +124212.42*T**(-1)	[44]
		G(Ti)(Fe)	3**G*HSER,(Fe)+3**G*HSER,(Ti) +89130- (-85500+410.041*T -73.553*T*Ln(T) -0.01017*T**2 +124212.42*T**(-1))	[27]
		G(Fe)(W)	-31100.4+376.7*T -70.434*T*Ln(T)	[28]

			-0.00492*T**2+166642*T**(-1)	
		G(W)(Fe)	246880 +368.28*T -73.5*T*Ln(T) -0.000298*T**2+100893*T**(-1)	[28]
		${}^{0}L$ (Fe,Ti)(Fe)	-35000	[44]
		${}^{0}L$ (Fe,Ti)(Ti)	-35000	[44]
		${}^{0}L$ (Fe)(Fe,Ti)	-35000	[44]
		${}^{0}L$ (Ti)(Fe,Ti)	-35000	[44]

Constituents in brackets occupy the same sublattice. Va indicates a vacant lattice site. [a]For the FCC_A1 and BCC_A2 (disordered) phases, the second sublattice represents interstitial sites. [b]The thermodynamic description here is combined with that for BBC_A2 in a single Gibbs energy expression for the BCC phase. This part forms the 'ordered contribution' to the Gibbs energy of the phase, and the BCC_A2, the disordered contribution. [c]*G*HSER,(Fe) represents the Gibbs energy of pure Fe in its reference state (the Standard Element Reference) [46].

As mentioned in the main text, the models used for the mu-phase in the Fe-W and the partial assessment of Fe-Ti-W [22] systems were slightly different (3 sublattices in Fe-Ti-W c.f. 4 sublattices in Fe-W). It was possible to use the 4 sublattice model here and still use the parameter from [22].